Strong coupling between a single nitrogen-vacancy spin and the rotational mode of diamonds levitating in an ion trap

T. Delord, L. Nicolas, Y. Chassagneux, and G. Hétet*

Laboratoire Pierre Aigrain, Ecole normale supérieure, PSL Research University, CNRS, Université Pierre et Marie Curie, Sorbonne Universités, Université Paris Diderot, Sorbonne Paris-Cité, 24 rue Lhomond, 75231 Paris Cedex 05, France

(Received 8 March 2017; published 7 December 2017)

A scheme for strong coupling between a single atomic spin and the rotational mode of levitating nanoparticles is proposed. The idea is based on spin readout of nitrogen-vacancy centers embedded in aspherical nanodiamonds levitating in an ion trap. We show that the asymmetry of the diamond induces a rotational confinement in the ion trap. Using a weak homogeneous magnetic field and a strong microwave driving we then demonstrate that the spin of the nitrogen-vacancy center can be strongly coupled to the rotational mode of the diamond.

DOI: 10.1103/PhysRevA.96.063810

I. INTRODUCTION

Experiments in the field of optomechanics have shown control of macroscopic mechanical oscillators very close to their ground state of motion [1]. These accomplishments provide great opportunities to observe quantum superpositions with macroscopic systems. Although progress is being made with room-temperature oscillators [2–4], the difficulty in most experiments is that they require cooling of the oscillators down to millikelvin temperatures or carefully engineered nanomechanical oscillators because they are clamped to a structure. Inspired by ideas for mechanical control of oscillating cantilevers using magnetic field-sensitive probes [5–9], trapped macroscopic objects coupled to single spins via magnetic-field gradients have been envisioned [10]. There, the mechanical support is completely removed so one could operate at room temperature and reach high-quality factors [11]. Further, the spins coupled to the massive object can be used to create matter-wave interference [12] and Schrödinger cat states where the spin is entangled with the collective oscillator motion [10,13].

Many experimental protocols are being explored to couple the center-of-mass mode of levitating objects to single spins, most of which use diamonds with embedded nitrogen-vacancy (NV) centers in dipole traps [10]. In recent experiments, however, despite the mechanical support being completely removed, light scattering from the optically levitated object significantly altered the photophysical properties of the NV centers [14–16]. Although advances have been made in this direction [17], many groups have indeed observed strong heating at low vacuum pressures, which quenches the NV photoluminescence [14,18,19]. On the other hand, scatter-free traps such as Paul traps and magnetogravitational traps allow one to reach a lower vacuum [20,21], although currently at a lower trapping frequency. One further difficulty with the hybrid proposals is that reaching strong coupling between a single spin and the center-of-mass mode implies high magnetic-field gradients, in the range of 10^5 to 10^7 T/m [6,13], which is very challenging.

In this paper, we present a scheme for strong coupling between a single spin and levitating nanoparticles that leverages most of these issues. First, we propose using a Paul trap for rotational confinement of charged aspherical nanodiamonds. Second, the rotational degree of freedom is coupled to the spin of embedded NV centers via homogeneous magnetic fields. The proposal makes use of the inherent quantization axis of the NV center together with the sensitivity of its spin energy levels to the magnetic field. We show that homogeneous magnetic fields in the range of tens of milliteslas (mT) are enough to enter the strong coupling regime for the rotational mode of prolate particles.

Figure 1 shows schematics of the proposal. A prolate diamond is levitating in a needle Paul trap. The coupling between the diamond rotational mode and the NV center relies on the control of its electronic spin in a homogeneous magnetic field. The NV centers in diamond consist of a substitutional nitrogen atom (N) associated with a vacancy (V) in an adjacent lattice site of the diamond matrix. This defect behaves as an artificial atom trapped in the diamond matrix and exhibits a strong photoluminescence in the red, which allows the detection of individual NV defects at room temperature. It is also possible to optically initialize and read out the electronic spin of the NV center thanks to the presence of a metastable level and an intersystem crossing [22]. Compared to single atoms, where the quantization axis is defined with respect to the B field, with NV centers, the ground-state spin-spin interaction sets a preferential quantization axis, namely, the N-V direction, as shown in the inset. This feature is the cornerstone of this proposal.

II. ROTATIONAL CONFINEMENT IN A PAUL TRAP

NV centers were detected with diamonds levitating in a Paul trap in [23] and [24]. In [24], the electronic spin resonance of nanodiamonds was further employed to experimentally demonstrate their angular stability. Here, we show that the rotation about two axes is ruled by a Mathieu equation so that the angle is stabilized, like the center of mass. To show this, let us consider the following time-dependent quadratic electric potential, $V_E(t) = \frac{\eta V(t)}{z_0^2}(z^2 - \frac{1}{2}x^2 - \frac{1}{2}y^2)$, where $V(t) = V_{\rm dc} + V_{\rm ac}\cos(\Omega t)$ is the voltage applied to the needle electrodes oscillating at a frequency $\Omega/2\pi$, z_0 is the distance between the two needles, and η an efficiency parameter that accounts for deviations from ideal hyperbolic

*gabriel.hetet@lpa.ens.fr

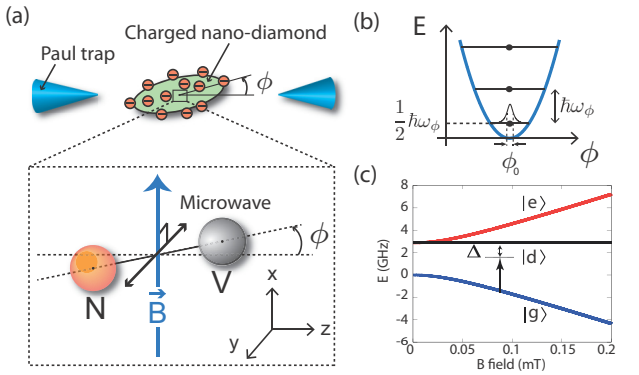

FIG. 1. (a) Schematics showing a prolate nanodiamond levitating in a needle Paul trap. The spin of a nitrogen-vacancy (NV) center inside the diamond senses the rotation of the particle in the presence of a transverse B field. (b) Harmonic potential energy as a function of the angle ϕ between the particle and the main trap axis, with rotational frequency ω_ϕ. (c) NV center ground-state level shifts in the presence of a transverse magnetic field. The arrow shows the microwave driving with detuning Δ from the $|g\rangle$ to the $|d\rangle$ transition.

electrode shapes [25]. To evaluate the rotational frequency, we take a particle with total surface charge Q and assume that the charge centroid coincides with the center of mass at all times.

One can then calculate the torque applied by the electric field to the particle. For an element of surface dS with charge dQ and in the fixed xyz frame the torque reads

$$d\vec{M} = \frac{\eta V(t)}{z_0^2}\begin{pmatrix} -3yx \\ 3xz \\ 0 \end{pmatrix} dQ. \tag{1}$$

This torque can then be integrated over the whole surface of the particle to obtain Euler's rotation equations. To factorize the dependency on the orientation of the particle, the integration is done in the rotating frame XYZ, whose axes are fixed to the particle and parallel to its principal axes of inertia. We consider the particle to be symmetric about its Z axis and hence use only two Euler angles ϕ_1 and ϕ_2 to define the XYZ frame: ϕ_1 for a first rotation of the initial frame xyz about the y axis and ϕ_2 for a second rotation of the rotated frame $x'y'z'$ about the rotated x' axis. The matrix allowing one to obtain XYZ from xyz is

$$R(\phi_1,\phi_2) = \begin{pmatrix} \cos\phi_1 & 0 & \sin\phi_1 \\ 0 & 1 & 0 \\ -\sin\phi_1 & 0 & \cos\phi_1 \end{pmatrix}\begin{pmatrix} 1 & 0 & 0 \\ 0 & \cos\phi_2 & -\sin\phi_2 \\ 0 & \sin\phi_2 & \cos\phi_2 \end{pmatrix}. \tag{2}$$

After changing the basis to integrate over the surface of the particle we find the total torque along the X and Y axis to be

$$M_X = \frac{3\eta V}{2z_0^2}\cos^2\phi_1 \sin(2\phi_2)\iint (Z^2 - Y^2)dQ$$

and

$$M_Y = \frac{3\eta V}{2z_0^2}\cos\phi_2 \sin(2\phi_1)\iint (Z^2 - X^2)dQ. \tag{3}$$

In the limit of small angles $\phi_1,\phi_2 \ll 1$, the Euler equations for the angles $\phi_{1,2}$ therefore become

$$I_x\ddot{\phi_1} - V(t)\left[\frac{3\eta}{z_0^2}\iint (Z^2 - X^2)dQ\right]\phi_1 = 0,$$
$$I_y\ddot{\phi_2} - V(t)\left[\frac{3\eta}{z_0^2}\iint (Z^2 - Y^2)dQ\right]\phi_2 = 0, \tag{4}$$

where $I_{x,y}$ are the moments of inertia relative to x and y, respectively. Equations (1) are Mathieu equations for angles ϕ_1 and ϕ_2. Within their stability conditions, they yield a harmonic confinement for both rotation angles of the particle, at secular frequencies

$$\omega_\mu = \frac{\Omega}{2}\sqrt{a_\mu + \frac{q_\mu^2}{2}}, \tag{5}$$

with dimensionless parameters

$$q_\mu = 3\frac{QS_\mu}{I_\mu}\frac{V_{ac}}{z_0^2}\frac{1}{\Omega^2} \quad \text{and} \quad a_\mu = -6\frac{QS_\mu}{I_\mu}\frac{V_{dc}}{z_0^2}\frac{1}{\Omega^2}, \tag{6}$$

where $\mu = X,Y$, $S_X = R_Z^2 - R_Y^2$, $S_Y = R_Z^2 - R_X^2$, and $R_\mu^2 = \iint \mu^2 dQ/Q$. At this stage, the calculations do not assume a homogeneous charge distribution.

Note that a small angle can initially be reached through damping of the surrounding gas as observed in [24] at atmospheric pressure or through parametric feedback under vacuum. Once within the small-angle approximation, the angular extension of the harmonic oscillator is due to the temperature of the surrounding gas and can be calculated using the equipartition of the energy. For prolate particles of 20- and 80-nm diameter as described below, we find $\sqrt{\langle\phi^2\rangle} = 0.16$ and 0.05 rad.

The rotational confinement depends not only on the charge-to-mass ratio and on the generated potential, as for the center of mass, but also crucially on the geometry of the particle. The factor QS_μ/I_μ in Eq. (3), which can be written $\iint(Z^2 - X^2)dQ/(\iiint Y^2 dm)$ for $\mu = Y$, can indeed be increased substantially using an asymmetric particle. A more significant advantage of using the rotational mode, however, comes from the possibility of strongly coupling to a single spin via a weak homogeneous magnetic field.

III. QUANTIZATION OF THE ROTATIONAL MODE

The rotational degree of freedom can be quantized like the center-of-mass mode. For a small rotation of the diamond about the y direction, the motional Hamiltonian can be linearized and takes the form

$$H_{\text{meca}} = \frac{1}{2}I_y\omega_\phi^2\hat{\phi}^2 + \frac{\hat{L}^2}{2I_y}, \tag{7}$$

where ω_ϕ is the rotational frequency, I_y the moment of inertia with respect to the y axis, and $\hat{L}$ the angular momentum. It can now be written in the form of a harmonic oscillator with the two variables $\hat{L}$ and $\hat{\phi}$. In analogy to the canonical conjugate observable $\hat{X}$ and $\hat{P}$ of the center-of-mass mode, one can define annihilation and creation operators $\hat{a}$ and $\hat{a}^\dagger$

such that $\hat{\phi} = \phi_0(\hat{a}^\dagger + \hat{a})$, where $\phi_0 = \sqrt{\hbar/(2I_y\omega_\phi)}$, and $\hat{L} = I_y\dot{\hat{\phi}} = iL_0(\hat{a}^\dagger - \hat{a})$, where $L_0 = \sqrt{\hbar I_y\omega_\phi/2}$ [26]. Figure 1(b) shows the harmonic potential for a small angle ϕ. A single quantum of motion will here have an angular extension ϕ_0 inversely proportional to the square root of the moment of inertia I_y.

IV. HAMILTONIAN FOR ROTATIONAL OPTOMECHANICS

Having quantized the rotational mode, we now turn to the estimation of the coupling strength between the NV center spin and the rotational mode. We take an NV center aligned with the Z axis, which rotates with the diamond around the y axis as depicted in Fig. 1(a). In the presence of a homogeneous transverse magnetic field along x, if the nanodiamond rotates, the projection of the spin component along the magnetic field is changed, thus providing a means to read out the angular motion. A torque can then also be applied to the diamond via the NV spin. The magnetic-field-dependent part of the Hamiltonian $\hat{H}_B = \gamma\vec{B}\cdot\hat{\vec{S}}$ describes the coupling of the spin $\hat{\vec{S}}$ to the transverse magnetic field B. Here γ is the gyromagnetic ratio of the NV electron spin. We take $\hat{S}_x$ and $\hat{S}_z$ the dimensionless spin operators along the X and Z rotating axes, and we get $\hat{H}_B = h\gamma B(\sin\hat{\phi}\hat{S}_z + \cos\hat{\phi}\hat{S}_x)$. Considering only first-order terms in $\hat{\phi}$, the magnetic Hamiltonian becomes

$$\hat{H}_B = h\gamma B\phi_0(\hat{a} + \hat{a}^\dagger)\hat{S}_z + h\gamma B\hat{S}_x. \tag{8}$$

The total Hamiltonian of the system then reads

$$\hat{H} = \hbar\omega_\phi\hat{a}^\dagger\hat{a} + \hat{H}_{\rm NV} + h\lambda_\phi(\hat{a} + \hat{a}^\dagger)\hat{S}_z, \tag{9}$$

where $\hat{H}_{\rm NV}$ is the Hamiltonian of the NV spin without the optomechanical coupling term and where the single quantum of motional shift is given by $\lambda_\phi = \gamma B\phi_0$. The NV Hamiltonian reads

$$\hat{H}_{\rm NV} = hD\hat{S}_z^2 + h\gamma B\hat{S}_x + \hbar\Omega_R\hat{S}_y\cos(\omega t). \tag{10}$$

The first term DS_z^2 arises from the spin-spin coupling between the two electrons in the ground states and lifts the degeneracy between the $|\pm0\rangle$ and the $|\pm1\rangle$ spin states. For the NV center, $D = 2.87$ GHz at room temperature. The second term, resulting from the transverse magnetic field, mixes the ground and excited electronic states $|0\rangle$, $|\pm1\rangle$ into the mixed state $|g\rangle$, $|d\rangle$, and $|e\rangle$ that is presented below. The third term describes the coupling between the NV electronic spin and a microwave that is linearly polarized along the y axis, at frequency ω and Rabi frequency Ω_R. We now diagonalize this Hamiltonian and show how this configuration allows us to obtain the coupling between the spin and the rotational mode. Note that the choice of the magnetic-field direction and microwave signal polarization is not critical and angles may be chosen to optimize the coupling rate [27].

In the absence of the microwave ($\Omega_R = 0$) the eigenstates of $\hat{H}_{\rm NV}$ are the mixed state $|d\rangle = (|-1\rangle - |1\rangle)/\sqrt{2}$, $|g\rangle = \cos\theta|0\rangle - \sin\theta|b\rangle$, $|e\rangle = \sin\theta|0\rangle + \cos\theta|b\rangle$, where $|b\rangle = (|-1\rangle + |1\rangle)/\sqrt{2}$, $\tan 2\theta = 2\gamma B/D$. The energies of these mixed states are $\omega_{e/g} = 2\pi D(1 \pm \sqrt{1 + (2\gamma B/D)^2})/2$, $\omega_d = 2\pi D$ and depend on the B field as shown in Fig. 1(c).

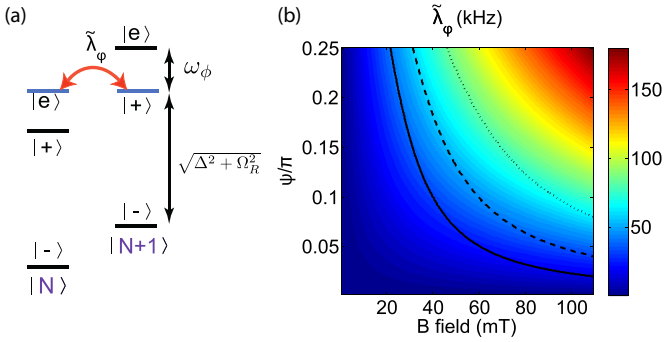

FIG. 2. (a) Level diagram and coupling between dressed spin states with rotational phonon numbers $N+1$ and N. (b) Coupling rate as a function of the B field and Ψ/π for $\omega_\phi/(2\pi) = 5$ MHz and a 20-nm-diameter prolate particle. Solid, dashed, and dotted black lines are the ψ parameter under resonant conditions as a function of the B field for Rabi frequencies of 250, 500, and 1000 MHz, respectively.

In the basis of these vectors, we have

$$\hat{S}_y = (\cos\theta|d\rangle\langle g| + \sin\theta|e\rangle\langle d| - \text{H.c.})/i.$$

In our case, we consider $\omega \sim \omega_{dg} = \omega_d - \omega_g \neq \omega_{ed}$ so that the microwave only drives the transition between the $|g\rangle$ and the $|d\rangle$ mixed states, as depicted in Fig. 1(a). We now move in a frame at the microwave frequency. In this frame, $\hat{H}_{\rm NV}$ reads

$$\hat{H}_{\rm NV} = \hbar/2\begin{pmatrix}-\Delta & 0 & 0\\ 0 & \Delta & 0\\ 0 & 0 & \omega_{e'}\end{pmatrix} + \hbar/2i\begin{pmatrix}0 & -\Omega_R & 0\\ \Omega_R & 0 & 0\\ 0 & 0 & 0\end{pmatrix}, \tag{11}$$

where $\Delta = \omega - \omega_{dg}$, $\omega_{e'} = \omega_e - (\omega + \omega_g + \omega_d)/2$, and the energy origin has been set to $(\omega_g + \omega_d)/2$.

The new eigenstates of this Hamiltonian are now $|e\rangle$, $|+\rangle = i\sin\psi|g\rangle + \cos\psi|d\rangle$, and $|-\rangle = -i\cos\psi|g\rangle + \sin\psi|d\rangle$, where $\tan 2\psi = \Omega_R/\Delta$ and with $\omega_{+/-} = \pm\sqrt{\Delta^2 + \Omega_R^2}/2$. In the new eigenstate basis $|+\rangle$, $|-\rangle$, $|e\rangle$, the Hamiltonian can be approximated by a Rabi Hamiltonian,

$$\begin{aligned}\hat{H} = {} & \hbar\omega_\phi\hat{a}^\dagger\hat{a} + \hbar\omega_+|+\rangle\langle+| + \hbar\omega_-|-\rangle\langle-| + \hbar\omega_{e'}|e\rangle\langle e|\\ & + h\tilde{\lambda}_\phi(\hat{a} + \hat{a}^\dagger)(|e\rangle\langle+| + \text{H.c.}),\end{aligned} \tag{12}$$

where $\tilde{\lambda}_\phi = \lambda_\phi\cos\theta\sin\psi$, which in turn can be reduced to a Jaynes-Cummings Hamiltonian under the condition that $\tilde{\lambda}_\phi \lesssim 10|\omega_e - \omega_+|/(2\pi)$ and if we neglect the off-resonant terms [28]. Here, we set the microwave such that only the states $|+,N\rangle$ and $|e,M\rangle$ (with $M - N = \pm1$, M and N being the phonon numbers) are resonant, i.e., $\omega_{e'} - \omega_+ = \omega_\phi$. In Eq. (12), the other terms $|+\rangle\langle-|$ and $|e\rangle\langle-|$ are neglected in the rotating-wave approximation.

Figure 2(a) depicts the $|+,N\rangle$ and $|e,M\rangle$ states under the resonant condition $\omega_{e'} - \omega_+ = \omega_\phi$: in the strong coupling regime, this Hamiltonian allows us to obtain a coherent exchange between rotational phonons and spin states at the rate $\tilde{\lambda}_\phi = \lambda_\phi\cos\theta\sin\psi$.

V. COUPLING RATE

In Fig. 2(b) the coupling rate $\tilde{\lambda}_\phi$ is plotted as a function of the magnetic field and the ψ parameter, which depend on the microwave settings Ω_R and Δ. It can be optimized by taking a resonant microwave ($\psi = \pi/4$) and a strong magnetic field. There is a practical limitation to accessing the area of this map, however: as the magnetic field is increased, the resonance condition ($\omega_{e'} - \omega_+ = \omega_\phi$) requires a large splitting $\sqrt{\Delta^2 + \Omega_R^2}$ between the $|+\rangle$ and the $|-\rangle$ states. Since it is technically challenging to increase $\Omega_R/2\pi$ above the gigahertz (GHz) range [29], one will have to increase Δ, therefore limiting oneself to lower ψ values. The ψ parameter needed to obtain the resonant condition as a function of the magnetic field given certain Rabi frequencies is plotted above $\tilde{\lambda}_\phi$ in Fig. 2(b). These curves show that for all three Rabi frequencies, the optimum of the coupling rate is obtained with a resonant microwave. We now turn to the optimization of $\tilde{\lambda}_\phi$ through the geometry of the particle.

A. Role of the geometry

Besides the NV spin, using the rotational mode also has a number of advantages that have been emphasized by several groups working on optical tweezers [30–32]. As we show here, reducing the size of the particle to obtain a better charge-to-mass ratio and engineer its shape dramatically increases the rotational confinement. The crucial parameters for attaining the strong coupling regime can be extracted from the formulas $\phi_0 = \sqrt{\hbar/2I_y\omega_\phi}$ and $\omega_\phi \sim \frac{QS_\mu}{I_\mu}\frac{V_{\rm ac}}{z_0^2}\frac{1}{\Omega}$. The angular frequency ω_ϕ must be higher than the width of the electron spin resonance to achieve any coherent manipulation. Also, ϕ_0 must be high enough in order for the phonon-photon coupling rate $\tilde{\lambda}_\phi = \lambda_\phi \cos\theta \cos\psi$ to be higher than all decoherence rates. Both ω_ϕ and ϕ_0 depend on parameters that are both intrinsic and extrinsic to the diamond. Because of the $\cos\psi$ term in $\tilde{\lambda}_\phi$, the Rabi frequency Ω_R has to be as large as possible with no detuning Δ. Here we take $\Omega_R/2\pi = 500$ MHz as a technical upper bound. This in turn limits the intensity of the B field we can use while achieving the spin-phonon resonance to $\sim$30 mT. The other extrinsic parameters such as the Paul trap parameters $V_{\rm ac}$, z_0, and Ω can be increased to tune the frequency ω_ϕ. Technical limitations will, however, set an upper bound: the Paul trap should not be lower than a few tens of microns, and reaching a voltage higher than a few thousand volts at high frequencies will be challenging. The intrinsic parameters of the diamond particle are then the only parameters that can be tuned.

The frequency that must be attained is determined by both the quality of the diamond and the distance of the NV center from the surface and, hence, by the diameter d of the considered diamond. However, one can see that decreasing the size of the diamond can considerably increase the trapping frequency. This is manifest in the fact that $\frac{QS_\mu}{I_\mu} = \frac{\sigma S S_\mu}{I_\mu}$ scales as $\frac{1}{d}$, provided the charge density on the diamond surface is independent of d. Then the factor $\frac{QS_\mu}{I_\mu}$ depends strongly on the geometry. To obtain a high ϕ_0, one also must have a low inertia momentum. This also points towards using small particles and highlights the relevance of the geometry.

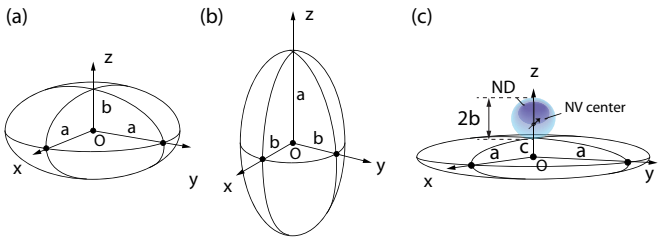

FIG. 3. Shapes of the proposed asymetric particles: (a) oblate ellipsoid, (b) prolate ellipsoid, and (c) composite particle formed by a diamond sphere deposited on a thin disk, approximated by an oblate ellipsoid.

In short, micron-size diamonds do not lend themselves easily to coherent manipulation since they are heavier, but they will retain the photophysical properties of bulk diamonds. Conversely, nanodiamonds have shorter coherence times than in the bulk but faster coupling rates can be reached. By tuning the aspect ratio of particles one can, however, find a compromise.

Three geometries have been envisioned and are depicted in Fig. 3: oblate and prolate ellipsoids, as well as composite particles formed by a diamond sphere deposited on a thin disk. The latter shape enables the choice of any material for the disk and, thus, optimization of the charge-to-mass ratio and trapping frequency independently of the diamond. For all shapes, the b and a parameters always correspond to the minimum and maximum particle radius, respectively. In Table I, the trapping frequencies and moment of inertia are calculated for these shapes. They are normalized with respect to the trapping frequencies (ω_0) and moment of inertia (I_0) of a sphere with the same radius b. It is indeed important to compare particles with the same minimum radius to ensure that the NV properties (which depend crucially on their distance from the surface) are the same. The rotational frequency is also compared to the center-of-mass mode $\omega_{\rm com}$, for the same b and for an aspect ratio $a/b = 2.5$. The trapping frequencies were calculated by integrating the torque over the surface of the ellipsoids, considering a homogeneous surface charge. Examining Table I, one sees that particles with a higher asymmetry and spatial extent experience a higher rotational trapping frequency. They, however, also have a greater moment of inertia, which will reduce the coupling

TABLE I. Comparison of the mechanical parameters of different particles shapes, as shown in Fig. 3 for the same b, the same aspect ratio $a/b = 2.5$, and the identical surface charge density. ω_0 and I_0 are the secular frequency of the center of mass and the moment of inertia of a sphere with radius b, respectively. For each considered particle, $\omega_{\rm com}$ and ω_ϕ are the secular frequencies of the center of mass and the rotational modes, respectively, and I_y is the moment of inertia.

Particle type	c/b	$\omega_{\rm com}/\omega_0$	ω_ϕ/ω_0	$\omega_\phi/\omega_{\rm com}$	I_y/I_0
Sphere	–	1	0	0	1
Oblate ellipsoid	–	0.64	1.8	2.9	23
Prolate ellipsoid	–	0.83	2.3	2.8	9
Composite	0.125	2.8	19	5.3	2.4
Composite	0.0625	3.3	27.6	6.3	1.2

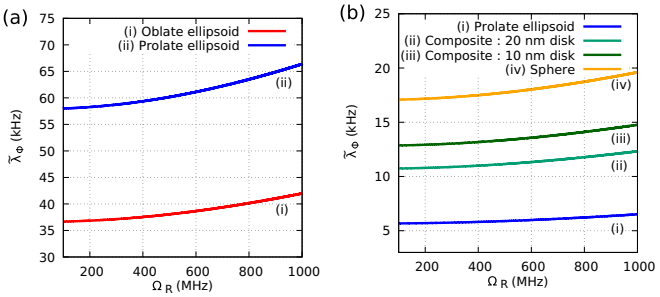

FIG. 4. Coupling rate $\tilde{\lambda}_\phi$ for nanodiamonds of different shapes (a) with radius $b = 20$ nm for prolate and oblate ellipsoids with rotational confinement $\omega_\phi = 5$ MHz and (b) with $b = 80$ nm and rotational confinement $\omega_\phi = 0.5$ MHz. The microwave is set at resonance with a varying Rabi frequency and the magnetic field is tuned to obtain resonant conditions. For example, at $\Omega_R/2\pi = 500$ MHz we have $B \sim 30$ mT. The aspect ratio of the proposed particles is $a/b = 2.5$ for all particles and $c/b = 1/8$ and $1/16$ for the composite 20- and 10-nm disks, respectively. The coupling rate with a zero-mass disk (i.e., for a sphere) is plotted as a limit for such particles (trace iv).

λ_ϕ. To both increase the trapping frequency and reduce the inertia momentum without reducing the size of the particle, the proposed composite particle, comprising a spherical diamond of size b within or deposited on a thinner disk of silica, allows us to considerably increase the confinement of the particle with a moment of inertia much smaller than those for simpler shapes, as can be seen in Table I.

We note that, even though advances have been made in engineering the shape of nanodiamonds, the proposed ellipsoidal particles are an approximation of the particle shapes in [33–35]. Reactive ion etching [35,36] is, however, quite adapted for rotational optomechanics, since diamonds can be engineered to form nanopillars that are close to prolate ellipsoidal particles.

Let us now estimate the spin-phonon coupling rate for the above particle geometries. We compare two particle sizes. In Fig. 4, the coupling rate $\tilde{\lambda}_\phi$ is plotted as a function of the Rabi frequency for the particle geometries described above, such as oblate, prolate, and composite particles. Figure 4(a) shows the coupling rate for particles with a radius $b = 20$ nm and an aspect ratio of $a/b = 2.5$ as a function of the Rabi frequency and with the magnetic field tuned to achieve resonant conditions. The coupling increases with the Rabi frequency as expected, since the higher it is, the higher can the magnetic field can be while still fulfilling the resonance condition. Here for a Rabi frequency $\Omega_R/2\pi = 500$ MHz and a magnetic field $B \sim 30$ mT, $\tilde{\lambda}_\phi$ ranges from 35 to 60 kHz. In Fig. 4(b) the considered particles are chosen to have radius $b = 80$ nm. Due to the high mass, the coupling rate for a prolate ellipsoid is then lower, barely exceeding 5 kHz. It can, however, be increased using a composite particle of a silica pancake-like shape with a nanodiamond deposited on top. The coupling strength will then depend crucially on how thin the disk of the composite particle can be.

B. Total number of charges

In order to reach significant trapping frequencies, the surface charges on the nanodiamond must be high enough, which in turn may yield charge fluctuations that will affect the NV spin coherence time. First, in order to obtain an order of magnitude for the needed total surface charge, we compute the trapping frequency for the needle trap. The curvature of and distance between the needles determine the confinement and the potential depth in both the radial and the axial plane [37]. The axial angular frequency ω_z of the harmonic pseudopotential is given by $\omega_z = |Q_{\rm tot}|V_{\rm ac}\eta/\sqrt{2}m\Omega z_0^2$, where $V_{\rm ac}$ is the peak-to-peak voltage applied between the electrodes and the far-distant surrounding ground, m the mass of the trapped particle, and η the efficiency factor, which accounts for the reduction in the trap potential compared to an analogous quadrupole trap with hyperbolic electrodes. $\Omega/2\pi$ is the trapping frequency and $Q_{\rm tot}$ is the total excess charge of the particle. One can then deduce the total surface charge needed to reach the two considered rotational frequencies given in Figs. 3(a) and 3(b). Taking a prolate nanodiamond particle with an aspect ratio of 2.5, we find, from Table I, the rotational mode to be about 3 times larger than the center-of-mass radial mode. We thus get

$$|Q_{\rm tot}| = \frac{2\sqrt{2}m\Omega z_0^2}{3\omega_\phi \eta V_{\rm ac}}.$$

We then take a distance between the electrodes of 10 μm, an efficiency parameter $\eta = 0.3$, a voltage $V_{\rm ac} = 5000$ V, and a trapping frequency of 5 MHz. In order to reach a trapping frequency of 0.5 MHz and with $b = 80$ nm, we find that at least 60 elementary charges must be present on the diamond surface. These charges can originate from remaining sp^2 layers or can be generated *in situ* using UV light.

VI. DECOHERENCE SOURCES

The so-called strong coupling regime is reached if the spin-phonon coupling rate exceeds the decoherence rates of both the spin and the considered mechanical oscillator modes. For the spin, this strong coupling condition translates to $T_1, T_2 \gg 1/\tilde{\lambda}_\phi$, where $T_2^{-1} = (2T_1)^{-1} + (T_2^*)^{-1}$, and $(T_2^*)^{-1}$ is the inhomogeneous decoherence rate due to the coupling between the NV spin and a nuclear spin bath or due to charge fluctuations.

A. Nuclear spin bath

For very shallow (5-nm-deep) NV centers, T_1 generally ranges from several hundreds of microseconds to milliseconds [38]; the main constraint for reaching the strong coupling regime is therefore the T_2^* time. Studies using dynamical decoupling sequences show that NV centers within 50-nm-diameter nanodiamonds synthesized through reactive ion etching [35] of CVD-grown diamonds should reach T_2 times of up to 200 μs using ^{12}C isotopically engineered diamonds [39,40]. It was indeed shown that the main source of the degradation of T_2 is the ^{13}C nuclear spin bath. For particles with a 20-nm minimum bulk radius, a $T_2 \sim 150$ μs would already allow entrance to the strong coupling regime. For particles with a 80-nm radius, T_2 is expected to be closer to bulk values and can attain $\sim$1.8 ms [39]. Looking at Fig. 3(b), $T_2 \gtrsim 1$ ms would already be sufficient to reach the strong coupling regime.

B. Charge fluctuations

Aside from assisting the rotational coupling, the charges may have detrimental effects on the electronic spin. First, surface charges have been shown to affect the NV^--to-NV^0 conversion. For the considered diamond diameters (>40 nm), however, this effect is not significant [41]. It was shown that the dominant source of electric noise under zero magnetic field is related to the optical illumination of the NV center for centers deeper than 100 nm, and the electric noise remains significantly smaller than the magnetic noise for the magnetic field of tens of milliteslas used in the proposed rotational optomechanics [42]. The electric-field noise contribution is expected to increase significantly only when the distance from the surface is below 10 nm, owing to the close proximity of fluctuating charges lying on the diamond surface [43]. If, in the end, surface charge fluctuations still cause decoherence to the NV spin, one could also expect that they will be modified, and possibly reduced, by the Paul trap. Due to the motional instability of the small electron masses, the trap may apply an effective outward force, potentially stabilizing the surface electrons and thus reducing the electric noise. The latter conjecture, however, remains to be checked experimentally or theoretically with a model dealing with the actual surface termination.

C. Spin polarization

In this paper, we do not touch upon phonon and spin state preparation and readout, which can be done using the present coupling scheme. One foreseeable concern is the transverse B field of NV centers, which degrades the spin polarization and readout efficacy by inducing spin mixing of the ground and excited spin states [44]. The optimum transverse magnetic field should thus be found for initialization and readout of the spin state.

The strong coupling condition itself, however, is unaffected by this spin mixing, as it does not rely on spin-selective nonradiative de-excitation. For the full protocol including rotational mode and spin preparation, spin-phonon coupling, and final phonon state readout, a sequence with an optimized time-dependent transverse magnetic field seems necessary and will be dealt with in a forthcoming paper.

VII. CONCLUSION

To conclude, we have shown how to benefit from the original spin properties of the NV center to obtain a rotational optomechanical coupling using a nanodiamond levitating in a Paul trap. We show how to enter the strong coupling regime for different particle sizes and shapes. This quantum optomechanical approach is promising in that it uses scattering-free trapping of nanodiamonds at room temperature and circumvents the necessity of employing very strong magnetic gradients [6,10]. In the longer run, this platform will enable efficient quantum control of macroscopic oscillators, paving the way towards Schrödinger cat states where the NV spin is entangled with the collective rotational motion of millions of atoms [10,13]. This novel architecture will, furthermore, open opportunities for studying fundamental phenomena in quantum optics and establishing building blocks of future quantum-based technologies.

Note added in proof. Recently, complementary work by Y. Ma and coworkers was presented in [27].

ACKNOWLEDGMENTS

We would like to acknowledge fruitful discussions with Peter Rabl. This research was partially funded by the French National Research Agency (ANR) through the SMEQUI project.

[1] M. Aspelmeyer, T. J. Kippenberg, and F. Marquardt, Rev. Mod. Phys. **86**, 1391 (2014).
[2] C. Reinhardt, T. Müller, A. Bourassa, and J. C. Sankey, Phys. Rev. X **6**, 021001 (2016).
[3] R. A. Norte, J. P. Moura, and S. Gröblacher, Phys. Rev. Lett. **116**, 147202 (2016).
[4] Y. Tsaturyan, A. Barg, E. S. Polzik, and A. Schliesser, Nat. Nanotechnol. **12**, 776 (2017).
[5] P. Treutlein, D. Hunger, S. Camerer, T. W. Hänsch, and J. Reichel, Phys. Rev. Lett. **99**, 140403 (2007).
[6] P. Rabl, P. Cappellaro, M. V. G. Dutt, L. Jiang, J. R. Maze, and M. D. Lukin, Phys. Rev. B **79**, 041302 (2009).
[7] O. Arcizet, V. Jacques, A. Siria, P. Poncharal, P. Vincent, and S. Seidelin, Nat. Phys. **7**, 879 (2011).
[8] S. Kolkowitz, A. C. Bleszynski Jayich, Q. P. Unterreithmeier, S. D. Bennett, P. Rabl, J. G. E. Harris, and M. D. Lukin, Science **335**, 1603 (2012).
[9] P.-B. Li, Z.-L. Xiang, P. Rabl, and F. Nori, Phys. Rev. Lett. **117**, 015502 (2016).
[10] Z. Yin, N. Zhao, and T. Li, Sci. China Phys. Mech. Astron. **58**, 1 (2015).
[11] D. E. Chang, C. A. Regal, S. B. Papp, D. J. Wilson, J. Ye, O. Painter, H. J. Kimble, and P. Zoller, Proc. Natl. Acad. Sci. USA **107**, 1005 (2010).
[12] M. Scala, M. S. Kim, G. W. Morley, P. F. Barker, and S. Bose, Phys. Rev. Lett. **111**, 180403 (2013).
[13] Z.-q. Yin, T. Li, X. Zhang, and L. M. Duan, Phys. Rev. A **88**, 033614 (2013).
[14] L. P. Neukirch, J. Gieseler, R. Quidant, L. Novotny, and A. N. Vamivakas, Opt. Lett. **38**, 2976 (2013).
[15] V. R. Horowitz, B. J. Alemán, D. J. Christle, A. N. Cleland, and D. D. Awschalom, Proc. Natl. Acad. Sci. USA **109**, 13493 (2012).
[16] M. Geiselmann, M. L. Juan, J. Renger, J. M. Say, L. J. Brown, F. J. G. de Abajo, F. Koppens, and R. Quidant, Nat. Nanotechnol. **8**, 175 (2013).
[17] A. C. Frangeskou, A. T. M. A. Rahman, L. Gines, S. Mandal, O. A. Williams, P. F. Barker, and G. W. Morley, arXiv:1608.04724.
[18] A. T. M. A. Rahman, A. C. Frangeskou, M. S. Kim, S. Bose, G. W. Morley, and P. F. Barker, Sci. Rep. **6**, 21633 (2016).

[19] T. M. Hoang, J. Ahn, J. Bang, and T. Li, Nat. Commun. **7**, 12250 (2016).
[20] T. Delord, L. Nicolas, M. Bodini, and G. Hétet, Appl. Phys. Lett. **111**, 013101 (2017).
[21] J.-F. Hsu, P. Ji, C. W. Lewandowski, and B. D'Urso, Sci. Rep. **6**, 30125 (2016).
[22] A. Gruber, A. Drábenstedt, C. Tietz, L. Fleury, J. Wrachtrup, and C. von Borczyskowski, Science **276**, 2012 (1997).
[23] A. Kuhlicke, A. W. Schell, J. Zoll, and O. Benson, Appl. Phys. Lett. **105**, 073101 (2014).
[24] T. Delord, L. Nicolas, L. Schwab, and G. Hétet, New J. Phys. **19**, 033031 (2017).
[25] W. Paul, Rev. Mod. Phys. **62**, 531 (1990).
[26] Because of its multivalued character, quantization of the canonical conjugate angle and orbital angular momenta has been a controversial debate [45]. Here, in the Paul trap, the angle is stabilized so that its value remains close to 0 at all times, thus ensuring that quantizing these variables can be done is analogy with the quantization of the position and momentum degrees of freedom.
[27] Y. Ma, T. M. Hoang, M. Gong, T. Li, and Z.-q. Yin, Phys. Rev. A **96**, 023827 (2017).
[28] D. Braak, in *Applications + Practical Conceptualization + Mathematics = Fruitful Innovation* (Springer, Berlin, 2016), pp. 75–92.
[29] G. Fuchs, V. Dobrovitski, D. Toyli, F. Heremans, and D. Awschalom, Science **326**, 1520 (2009).
[30] S. Kuhn, A. Kosloff, B. A. Stickler, F. Patolsky, K. Hornberger, M. Arndt, and J. Millen, Optica **4**, 356 (2017).
[31] B. A. Stickler, S. Nimmrichter, L. Martinetz, S. Kuhn, M. Arndt, and K. Hornberger, Phys. Rev. A **94**, 033818 (2016).
[32] T. M. Hoang, Y. Ma, J. Ahn, J. Bang, F. Robicheaux, Z.-Q. Yin, and T. Li, Phys. Rev. Lett. **117**, 123604 (2016).
[33] P. Appel, E. Neu, M. Ganzhorn, A. Barfuss, M. Batzer, M. Gratz, A. Tschöpe, and P. Maletinsky, Rev. Sci. Instrum. **87**, 063703 (2016).
[34] P. Andrich, B. J. Alemán, J. C. Lee, K. Ohno, C. F. de las Casas, F. J. Heremans, E. L. Hu, and D. D. Awschalom, Nano Lett. **14**, 4959 (2014).
[35] M. E. Trusheim, L. Li, A. Laraoui, E. H. Chen, H. Bakhru, T. Schröder, O. Gaathon, C. A. Meriles, and D. Englund, Nano Lett. **14**, 32 (2013).
[36] E. Neu, Appl. Phys. Lett. **104**, 153108 (2014).
[37] L. Deslauriers, S. Olmschenk, D. Stick, W. K. Hensinger, J. Sterk, and C. Monroe, Phys. Rev. Lett. **97**, 103007 (2006).
[38] T. Rosskopf, A. Dussaux, K. Ohashi, M. Loretz, R. Schirhagl, H. Watanabe, S. Shikata, K. M. Itoh, and C. L. Degen, Phys. Rev. Lett. **112**, 147602 (2014).
[39] G. Balasubramanian, P. Neumann, D. Twitchen, M. Markham, R. Kolesov, N. Mizuochi, J. Isoya, J. Achard, J. Beck, J. Tissler *et al.*, Nat. Mater. **8**, 383 (2009).
[40] J. R. Maze, J. M. Taylor, and M. D. Lukin, Phys. Rev. B **78**, 094303 (2008).
[41] L. Rondin, G. Dantelle, A. Slablab, F. Grosshans, F. Treussart, P. Bergonzo, S. Perruchas, T. Gacoin, M. Chaigneau, H.-C. Chang *et al.*, Phys. Rev. B **82**, 115449 (2010).
[42] P. Jamonneau, M. Lesik, J. P. Tetienne, I. Alvizu, L. Mayer, A. Dréau, S. Kosen, J.-F. Roch, S. Pezzagna, J. Meijer *et al.*, Phys. Rev. B **93**, 024305 (2016).
[43] M. Kim, H. J. Mamin, M. H. Sherwood, K. Ohno, D. D. Awschalom, and D. Rugar, Phys. Rev. Lett. **115**, 087602 (2015).
[44] J. Tetienne, L. Rondin, P. Spinicelli, M. Chipaux, T. Debuisschert, J. Roch, and V. Jacques, New J. Phys. **14**, 103033 (2012).
[45] H. A. Kastrup, Phys. Rev. A **73**, 052104 (2006).